

# Gravitational Microlensing of a Reverberating Quasar Broad Line Region – I. Method and Qualitative Results

H. Garsden, N. F. Bate and G. F. Lewis\*

*Sydney Institute for Astronomy, School of Physics, A28, The University of Sydney, NSW, 2006, Australia*

Accepted –. Received –; in original form 14 Jun 2011

## ABSTRACT

The kinematics and morphology of the broad emission line region (BELR) of quasars are the subject of significant debate. The two leading methods for constraining BELR properties are microlensing and reverberation mapping. Here we combine these two methods with a study of the microlensing behaviour of the BELR in Q2237+0305, as a change in continuum emission (a “flare”) passes through it. Beginning with some generic models of the BELR – sphere, bicones, disk – we slice in velocity and time to produce brightness profiles of the BELR over the duration of the flare. These are numerically microlensed to determine whether microlensing of reverberation mapping provides new information about the properties of BELRs. We describe our method and show images of the models as they are flaring, and the unlensed and lensed spectra that are produced. Qualitative results and a discussion of the spectra are given in this paper, highlighting some effects that could be observed. Our conclusion is that the influence of microlensing, while not strong, can produce significant observable effects that will help in differentiating the properties of BELRs.

**Key words:** gravitational lensing: micro – quasars: individual: Q2237+0305 – galaxies: structure – broad line region – methods: numerical

## 1 INTRODUCTION

The geometry and kinematics of quasar broad emission line regions (BELRs) are currently poorly constrained. This region is too small to be resolved with current generation telescopes, so we must rely on indirect techniques to probe its structure. The most prominent technique in use is reverberation mapping (Blandford & McKee 1982; Peterson 1993), however gravitational microlensing is a promising alternative (e.g. Nemiroff 1988; Schneider & Wambsganss 1990; Lewis et al. 1998; Abajas et al. 2002; Lewis & Ibata 2004; Abajas et al. 2007; O’Dowd et al. 2011; Sluse et al. 2011). In this paper, we discuss combining the two techniques, and conduct a numerical analysis of reverberation mapping in a gravitationally microlensed quasar, using several generic BELR models.

Perhaps the most prominent feature of quasar spectra are their broad emission lines. The line broadening is thought to be caused by the Doppler motions of the BELR gas, sometimes giving rise to line widths of up to tens of

thousands of kilometres. The absence of [OIII] $\lambda\lambda$ 4364, 4959, 5007 lines in quasar spectra, and the presence of the strongly non-permitted CIII] $\lambda$ 1909 line, allow us to infer electron densities in the BELR that suggest filamentary or clumpy structure. It is therefore natural to consider the BELR to consist of clouds of gas radiating at their thermal width, undergoing bulk motions large enough to produce the observed emission line widths.

Most of the information we have on the kinematics and structure of this region comes from reverberation mapping measurements. These experiments observe the response of the BELR to variations in the continuum flux from the active galactic nucleus (AGN). If there is a sudden increase in flux in the continuum, which we term a “flare”, this propagates through the BELR as an expanding shell and is re-emitted by the material it passes through. At the simplest level, reverberation mapping provides a measurement of the radius at which the emitting BELR gas is located. These measurements suggest stratification of the BELR, since higher ionisation lines such as CIV are emitted at radii closer to the source than lower ionisation lines such as CIII] (Peterson 1997). They also allow for the calculation of central black hole masses, under the assumption that virial motions dominate the BELR velocity structure (see for example Peterson et al. 2004; Bentz et al. 2009).

Recently, sampling rate and data quality have begun

\* E-mail: hgar7294@uni.sydney.edu.au (HG); nbate@sydney.usyd.edu.au (NFB); geraint.lewis@sydney.edu.au (GFL). Research undertaken as part of the Commonwealth Cosmology Initiative (CCI: www.thecci.org), an international collaboration supported by the Australian Research Council.

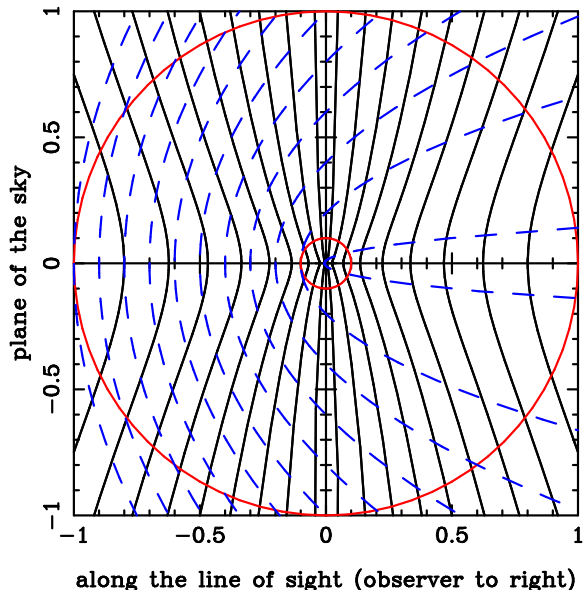


**Figure 1.** A projection of lines of constant time delay (dashed blue) and line-of-sight velocity (solid black) in a broad-line region during a flare, with the observer to the right of the plot. The constant time delay surfaces progress from right to left over time. The radial velocities increase out from the origin, via Equation 2 with  $p = 0.5$ . The red lines superimpose the inner and outer radius of a circular BELR. The axes are in units normalized to a radius of 1.

to reach a level where velocity-resolved time lags across broad emission lines can be measured (Horne et al. 2004; Bentz et al. 2008; Denney et al. 2009; Bentz et al. 2010). This was the original promise of the reverberation mapping technique: mapping the emissivity and velocity structure of the BELR. The results so far are ambiguous, indicating orbital, inflowing and outflowing bulk motion of the BELR gas (see especially Denney et al. 2009 and references therein). The interpretation of these signals remains problematic, but new methods, such as using Bayesian inference to iteratively converge on BELR parameters from light curves (Pancoast, Brewer, & Treu 2011; Brewer et al. 2011), will help to remove some of the ambiguities.

So far, reverberation mapping experiments have been mostly limited to low redshift, low luminosity AGN. The one notable exception is S5 0836+71, a redshift  $z = 2.172$  quasar with a tentative detection of a reverberation mapping time delay of 595 days in the observer’s frame (Kaspi et al. 2007). This was the result of approximately 5 years ( $\sim 1.2$ – $1.5$ yr in the quasar rest frame) spectroscopic monitoring of 6 high-redshift objects. Amongst other complications, high luminosity AGN have slower and smaller continuum variations than their low luminosity counterparts.

A complementary technique for constraining the detailed kinematic and geometric structure of the BELR is gravitational microlensing. In this scenario, a background quasar is multiply imaged by a foreground galaxy. Stars and other compact matter in the lensing galaxy can (de)magnify different regions of the BELR. Gravitational microlensing as a probe of BELR structure was first discussed in Nemiroff (1988), where the effect of a single low mass star was considered on a range of kinematical models for the

BELR. This work focused on broad emission line shapes. Schneider & Wambsganss (1990) noted that line shape is a difficult diagnostic to use, since they can vary considerably between sources, and within sources over time. Instead, they suggested comparisons between images in the same lensing system, since the underlying line profile should be identical, but the microlensing-induced variations are uncorrelated between images.

Subsequent theoretical analyses of the effect of microlensing on quasar BELRs were undertaken by Abajas et al. (2002), and Lewis & Ibata (2004). Both found that broad emission line profiles could be significantly affected by microlensing. Lewis & Ibata (2004) noted that spectroscopic monitoring of lensed quasars is required for obtaining detailed morphology of the BELR. Until very recently, this sort of expensive observational campaign has not been feasible. However, newer techniques such as cheap, efficient photometric observations of reverberation mapping (Chelouche & Daniel 2011) have been proposed as an alternative.

Some applications of gravitational microlensing analysis to actual BELR observational data have been made. Lewis et al. (1998) demonstrated that the BELR of Q2237+0305 was undergoing microlensing through measurements of line equivalent widths, and Wayth, O’Dowd & Webster (2005) used IFU data to constrain the size of the CIII]/MgII broad emission line region in the same quasar, finding it had a radius of  $\sim 0.06h_{70}^{1/2}$  pc.

More detailed spectroscopic analyses of broad emission lines in Q2237+0305 were undertaken by O’Dowd et al. (2011) and Sluse et al. (2011). O’Dowd et al. (2011) detected a differential microlensing signal across the CIII] emission in a single epoch of data. The data were compared to an outflowing and an orbital model of the BELR, and were found to favour the orbital model. Sluse et al. (2011) instead focused on a variety of techniques for analysing the lines directly, such as multi-component decomposition. They measured the sizes of the CIII] and CIV emission regions, and found that each line was emitted from two spatially distinct regions: a compact high velocity component, and a larger low velocity component. The half-light radius of the CIV region was found to be  $\sim 0.06$  pc. These results were also consistent with a BELR dominated by virial motions.

SDSS J1004+4112 has also been the subject of several observations. Richards et al. (2004) found enhancement of the blue wings of some emission lines in SDSS J1004+4112 that were attributed to microlensing. The blue wing enhancement was also observed by Gómez-Álvarez et al. (2006), but the absence of other microlensing-induced changes suggested intrinsic variability may be the cause. The latter has been supported by Lamer et al. (2006), who suggest it provides a better explanation than microlensing for differences in X-ray and UV variability. On the other hand, Ota et al. (2006) supports the microlensing hypothesis for X-ray flux anomalies and differences between X-ray and optical. Abajas et al. (2007) attempted to reproduce the blue wing enhancement numerically, using a biconical BELR model, and found that it could reproduce the observed signal, albeit with a low probability. Clearly, there is more work to be done to confirm microlensing, and BELR microlensing, in this system.

A lensed quasar that does show strong evidence of

BELR microlensing is SDSS J0924+0219, based on flux anomalies, in both the continuum spectra and broad-emission lines, between the different lensed images. The observations were made by Keeton et al. (2006) who derive a BELR size of  $\sim 9$  light days in this quasar.

The above microlensing analyses all assumed that the BELR emission was constant and unvarying. In this paper, we relax this assumption and explore the possibility of using gravitationally lensed quasars to perform reverberation mapping experiments. Using numerical microlensing techniques we model a flare passing through a BELR and observe the unlensed and lensed spectrum at several time intervals during the flare. We discuss reverberation and numerical microlensing in Section 2. In Section 3, we discuss the method used to obtain the data in this and subsequent papers. Results of the simulations are presented in Section 4. In Section 5 we discuss some of the effects produced by the microlensing of a flare. Our conclusions, and some implications for future work, are presented in Section 6.

Throughout this paper, a cosmology with  $H_0 = 70 \text{ km s}^{-1} \text{ Mpc}^{-1}$ ,  $\Omega_m = 0.3$  and  $\Omega_\Lambda = 0.7$  is assumed.

## 2 BACKGROUND

### 2.1 Broad emission-line region

In line with previous BELR microlensing analyses (particularly Abajas et al. 2002 and Lewis & Ibata 2004), we make use of the BELR models of Robinson (1995) to specify properties of a BELR. These models are not intended to be physically realistic. Rather, they focus on a few key features of the BELR: the velocity distribution of the BELR clouds, their emissivity, and the BELR size and orientation.

The BELR is assumed to consist of many clouds that re-radiate emission from the core. We adopt the following independent power-law relationships for the emissivity  $\epsilon$  and the magnitude of the velocity  $v$  of the emitting clouds in the BELR:

$$\epsilon = \epsilon_0 \left( \frac{r}{r_0} \right)^\beta \quad (1)$$

and

$$v = v_0 \left( \frac{r}{r_0} \right)^p \quad (2)$$

where  $r_0$  is the inner radius of the cloud system.

The efficiency with which the individual BELR clouds reprocess incoming radiation is assumed to be a smooth power-law function of radius. The volume density is also assumed to be a power-law function of radius. These two power-laws are implicitly combined into Equation 1 so that, for a suitable choice of  $\beta$  and  $\epsilon_0$ , the equation can be used as the flux at a distance  $r$  from the core. We assume that the number of clouds is large enough to approximate a smooth distribution. The clouds are assumed to emit isotropically, which implies that either the gas is optically thin or the BELR clouds are illuminated uniformly by diffuse ionising radiation. This assumption is almost certainly incorrect (see Robinson 1995 for details), however it is made here for the sake of simplicity. The clouds are also assumed to re-radiate emission received only from the core, and not from other clouds. This is also incorrect since clouds may excite each other, but we also ignore that here.

The kinematic properties of the BELR are responsible for the line-broadening via Equation 2, and, with the morphology and emission of the BELR, determine the spectrum. Different values of  $p$  in Equation 2 can considerably alter the spectrum – see Abajas et al. (2002) for examples. The direction of the velocity may be inflowing, outflowing, or orbital. The non-linear nature of Equation 2 also indicates that inflows and outflows are radially accelerating or decelerating.

### 2.2 Reverberation mapping

A flare in the AGN continuum can be used to map the BELR as the flare reverberates through it (Kaspi et al. 2007). Of particular significance is the time delay between the continuum flare and its appearance in and through the BELR, which allows the BELR size to be measured (Peterson 1993). Suppose at time  $\tau = 0$  a flare is emitted from the centre of the BELR ( $r = 0$ ). It travels outward at the speed of light, causing the BELR gas to brighten as it passes. In spherical polar coordinates ( $\phi$  is the zenith angle), the time at which a cloud is seen to flare by an observer is described by the following relationship:

$$\tau = \left( \frac{r}{c} \right) (1 - \cos\theta \sin\phi). \quad (3)$$

Although the flare propagates radially outwards, the observer sees the BELR brighten initially along the line-of-sight. The flare then appears to expand to cover the BELR until it diminishes again to the line-of-sight. At each time the observer is viewing a paraboloid surface spreading away from the observer through the BELR (Horne et al. 2004). Figure 1 depicts some of these properties with a side on view of a spherical BELR with  $p = 0.5$  in Equation 2, and the observer to the right. The red lines are the inner and outer radius of the BELR. The blue lines are lines of constant time delay, and they move from right to left over time. Also shown are lines of constant line-of-sight velocity (black), where the smallest velocity is at the vertical-axis, and increasing velocities to the left and right.

### 2.3 Numerical microlensing

When a quasar is gravitationally lensed by a foreground galaxy, multiple quasar images are produced due to the overall gravitational potential of the galaxy. These are magnified and distorted, and usually not resolvable into substructure. Modelling the location and magnifications of the images can be done analytically by assuming a smooth mass distribution for the lensing galaxy, which generates two key parameters for the mass distribution responsible for the images: the convergence ( $\kappa$ ), and shear ( $\gamma$ ). The convergence specifies the mass density in the vicinity of a light ray, the shear incorporates the effect of the overall mass distribution of the lensing galaxy.

The quasar moves relative to the line-of-sight from the observer to the lensing galaxy, and as it moves the structure within the galaxy – stars, planets, clouds, etc. – shifts relative to the light paths producing the quasar images. This can cause the images to fluctuate in magnification, an effect that is called “microlensing”. Microlensing has been observed in many lensed quasars (e.g. Walsh et al. 1979; Huchra et al.

1985; Turner et al. 1989; Myers et al. 1999; Inada et al. 2005; Abajas et al. 2007; Kayo, Inada, Oguri et al. 2010).

To model microlensing, the substructure in the lens galaxy must be taken into account, and since there are very many compact objects, microlensing is modelled numerically. Using the parameters above, compact objects and smooth matter are generated and light rays fired through them to calculate the deflections. It is computationally easier and more efficient to fire the rays from the observer through the lens to the plane of the source – this is called “inverse ray-tracing”. The rays hit a pixelized source plane behind the galaxy and are counted for each pixel; the number of rays reaching a pixel is the change in magnification, due to microlensing, of a pixel-sized source at that location. The result of inverse ray-tracing is a magnification map generated for each quasar image; Figure 2 shows the map for image A in Q2237+0305 that is used in this work. The map represents an area of sky over which a pixel-sized quasar source may be located; the mean magnification of the map is the magnification of the quasar image. Bright areas are where the quasar will be magnified, dark areas are where it will be demagnified, relative to the mean. These regions are separated by lines where the magnification becomes formally infinite, these are called “caustics”.

Quasars may be larger than a pixel. Extended sources such as these are modelled by convolving a source profile with the magnification map, producing another map representing the microlensing of the source. In microlensing, small sources exhibit the most variability in magnification, as large sources will blur the sharpness of the magnification map (Lewis & Ibata 2006; Bate et al. 2007). Sources of different shapes and sizes (Mortonson et al. 2005) may be magnified differently at different locations on the map because they lie over different regions of magnification. Similarly if the source is emitting different wavelengths from different locations, the spectrum may be altered (Wambsganss & Paczynski 1991; Mosquera et al. 2009) because the locations within the source profile may be magnified differently. This chromatic microlensing can be modelled by convolving a region of one wavelength with the magnification map, doing that for many regions, and reconstructing the microlensed spectrum. It will be used to study the effect of microlensing on our BELR models because the velocity varies by location over the BELR, so for certain locations on the map chromatic microlensing will be present.

Sources of similar size, or smaller, than the characteristic size scale used in microlensing – the Einstein Radius (ER) – will be more susceptible to microlensing (Wyithe, Webster, & Turner 2000). The Einstein Radius ( $\eta_0$ ) is derived from the mass of a single point lens and distances from the observer to the lens and to a point source:

$$\eta_0 = \sqrt{\frac{4GM}{c^2} \frac{D_{os} D_{ls}}{D_{ol}}}, \quad (4)$$

where  $G$  is the gravitational constant,  $M$  is the mass of the lens and  $D_{xy}$  refers to the angular diameter distance between  $x$  and  $y$ ; the subscripts  $s, l$ , and  $o$  representing source, lens, and observer respectively. In Q2237+0305, with a distance to the lens of  $z_L = 0.0394$ , and to the source of  $z_S = 1.695$ , and for a point lens of 1 Solar mass ( $M_\odot$ ), the Einstein Radius is 0.06 pc.

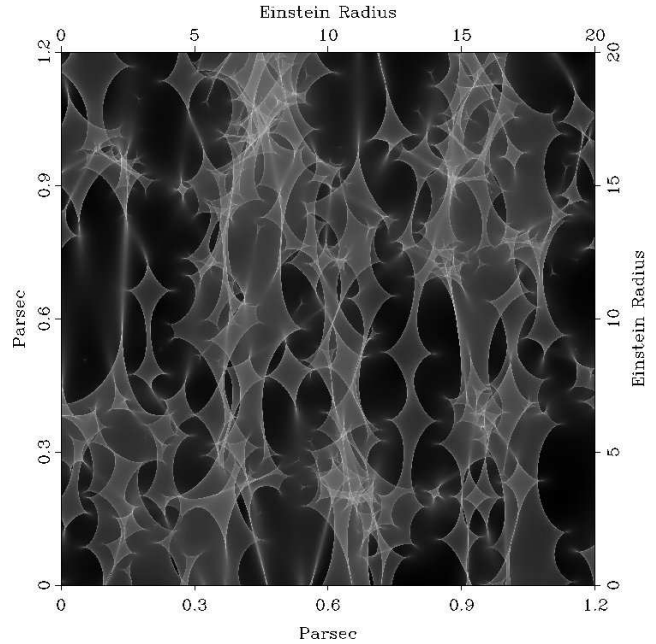


**Figure 2.** A magnification map generated for image A in Q2237+0305, and used in this paper. The brightness at a location indicates the magnification, due to microlensing, of a pixel-sized source situated at that location. Bright areas indicate high magnification, dark areas indicate low magnification, relative to the mean magnification of image A. The map was generated using a convergence  $\kappa = 0.36$  and shear  $\gamma = 0.40$ . The map covers a region in the source plane of  $1.2 \times 1.2$  pc<sup>2</sup> ( $20 \times 20$  ER<sup>2</sup>) at a resolution of 10000<sup>2</sup> pixels.

### 3 METHOD

We use Q2237+0305 for our lensed system as it is one of the most monitored lensed quasars (Udalski et al. 2008), and it is an attractive laboratory for microlensing studies because it has a large Einstein Radius and therefore high microlensing variability (Kayser & Refsdal 1989). While not a target of study for reverberation mapping, as significant BELR variability has not been reported, its BELR is one of the most studied (Lewis & Ibata 2004, 2006; Wayth et al. 2005; O’Dowd et al. 2011; Sluse et al. 2011, eg.), and will continue to be so (Mosquera & Kochanek 2011). We use it for illustrative purposes here. We generate source models for the BELR in Q2237+0305 that are sliced by time and velocity as a flare is propagating through the BELR. The slices are microlensed, and combined into a time-varying spectrum over the lifetime of the flare.

#### 3.1 Magnification Maps

For this paper we focus upon image A of Q2237; in a later contribution we will expand this to consider all images in this system. The magnification map we have generated for this image is shown in Figure 2. The convergence and shear values used are  $\kappa = 0.36$ ,  $\gamma = 0.4$  (Schmidt, Webster & Lewis 1998). We generate 1,575 objects with 1  $M_\odot$  masses for the lens, and no smooth matter, as the images are located in the bulge where stellar matter dominates. We use the inverse ray-tracing method developed by Wambsganss (1990, 1999) and Garsden & Lewis (2010) to fire the rays. The width of

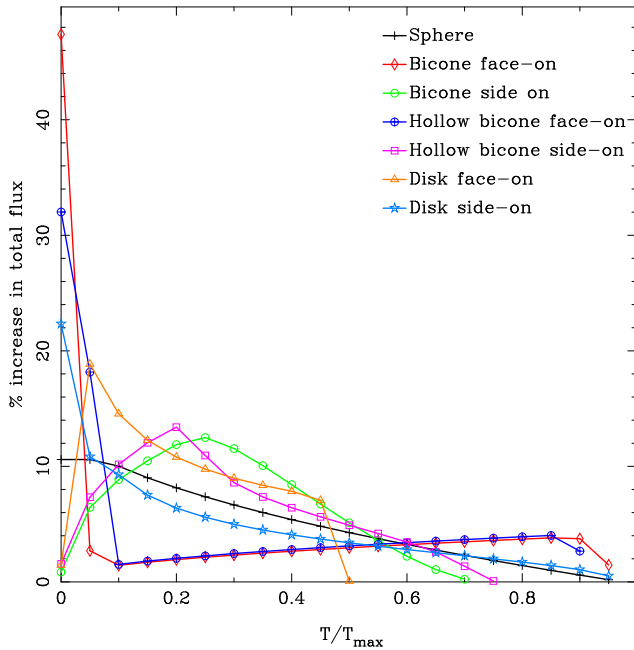


**Figure 5.** Change in observed BELR brightness over time in a flaring BELR, for the models at several orientations, with the flaring material having twice the emission than it does in its quiescent state. The vertical axis is the percentage increase in flux of the total BELR due to the flare, the horizontal axis is the time that has passed. Time has been binned into intervals that are 5% of the flare lifetime. Side-on orientations are inclined by  $90^\circ$ .

the map is 20 ER (1.2 pc) at a pixel resolution of  $10000^2$  pixels, or 0.002 ER (0.00012 pc) per pixel.

### 3.2 Model profiles

We use four different source models, three taken from Abajas et al. (2002): the sphere, disk, and bicone. There is also increasing evidence for a disk-wind model (Elvis 2000; Peterson 2006), which adds a funnel to the disk. For this paper and for simplicity we will implement a hollow bicone as the funnel, and examine it separately from the disk. In future work a full “disk-wind” model can be implemented by combining the disk and the hollow bicones.

We set the size of the models to be 1 ER = 0.06 pc, in line with sizes measured previously by Wayth et al. (2005) and Sluse et al. (2011). The models are oriented and projected onto the sky to produce a source profile for microlensing. All models have an inner radius of 10% of the total radius, i.e.  $r_0 = 0.1 r_{BELR}$  in Equation 1, where  $r_{BELR}$  is the outer radius of the BELR. The BELR material is transparent, and at each point emits with flux given by Equation 1, with  $\beta = -1.5$ . The models are described below.

#### 3.2.1 Sphere

The sphere is the simplest model, and is depicted in Figure 3(a). The material is inflowing, with  $p = 0.5$  in Equation 2, so that it is decelerating.

#### 3.2.2 Bicones

Two mirror-image cones are cut out from the sphere to form a biconical structure. The opening angle of the cones is  $30^\circ$ . The cones may be either solid, or hollow, in the latter case consisting of a conical shell where the shell wall has an opening angle of  $3^\circ$ . The direction of velocity is reversed so that the inflow becomes an accelerating outflow. The hollow cone is intended to be combined with the disk to form a disk-wind model, in which case it should have a rotational velocity component, but that is not used here. The cones may be inclined and then rotated on the plane of the map, with the anchor point the midpoint between the bicones. An inclination of  $0^\circ$  means that one of the cones is pointing directly towards the observer, and the other is pointing away. The rotation of the model is specified as a rotation angle (RA), where  $0^\circ$  rotation is pointing down the page on the magnification map in Figure 2, and  $90^\circ$  is pointing to the right. Figure 3(b) depicts the solid cones, inclined by  $90^\circ$ , RA =  $0^\circ$ . Figure 3(c) is slightly more complex, it shows the hollow cones, inclined by  $35^\circ$ , RA =  $45^\circ$ .

#### 3.2.3 Keplerian Disk

This model is a flat rotating disk with the BELR material in Keplerian orbits, so  $p = -0.5$  in Equation 2. The thickness of the disk is 1% of the outer radius. Like the bicones, the disk can be oriented with respect to the observer. By convention, an inclination of  $0^\circ$  is face-on. Figure 3(d) shows the disk inclined by  $45^\circ$ , RA =  $45^\circ$ .

### 3.3 Flaring

Within a certain time interval some material will be observed to be flaring. That material can be found based on the temporal properties of the flare discussed in Section 2.2. The emissivity of the material is increased from  $\epsilon$  (Equation 1) to  $k\epsilon$ . A suitable value for  $k$  must be chosen; Kaspi et al. (2007) have observed increases of 10-70% in the total BELR flux in several quasars at some (unknown) time during a flare. If we numerically determine the flux over time for a flare in all the models, at some different orientations, when  $k = 2$ , the result is shown in Figure 5. The horizontal axis is the percentage of the lifetime of the flare, the vertical axis is the percentage increase in flux of the BELR.

This shows that the most increase in brightness occurs in the early stages of the flare, due to the time delay surface moving away from the observer as depicted in Figure 1. The face-on cones show the biggest increase because the material along the line-of-sight is observed to flare first and this is a substantial amount of the total material in the face-on cones. The side-on orientations brighten later as they have less material along the line-of-sight. To estimate a flux increase for our models, we use the sphere, which has a increase of 10%, roughly the mean of all the models. To be consistent with the observations of Kaspi et al. (2007), we conservatively set  $k = 5$  for all models, which produces an increase of 50% in the sphere in the early stages.

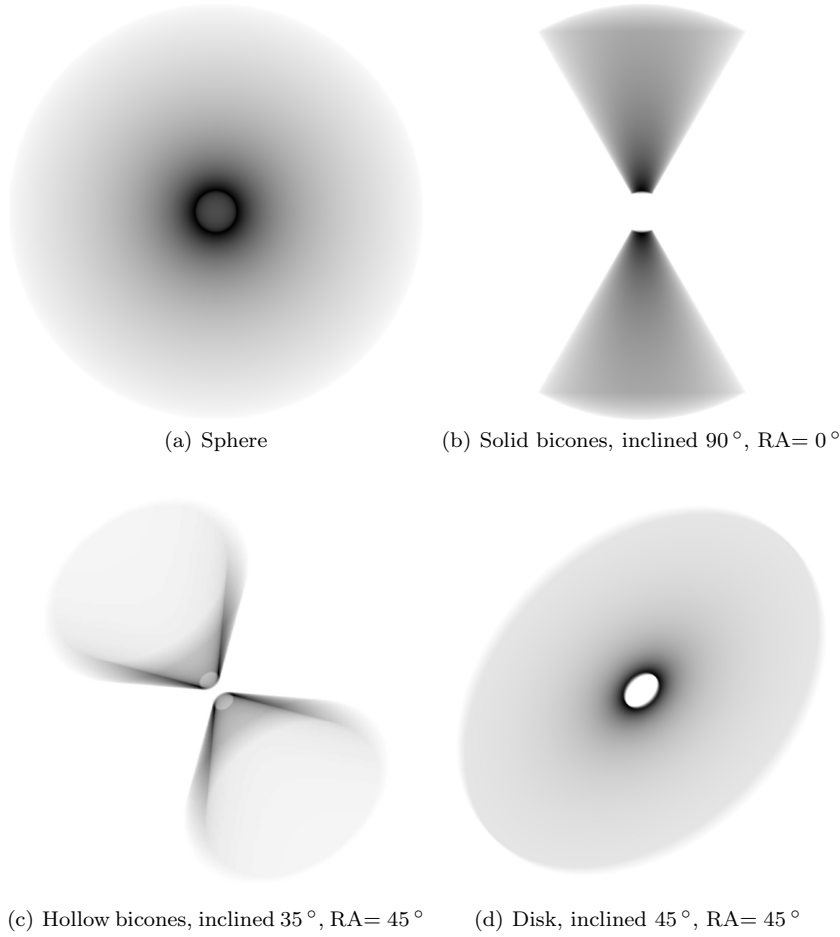


**Figure 3.** The source models used in this study. (a) is a sphere of uniformly distributed, transparent, inflowing material. (b) consists of two cones, with an opening angle of  $30^\circ$ , cut from the sphere in (a), and with the material outflowing. (c) is created from (b) by hollowing out the cones and replacing the surface with a shell wall that has an opening angle of  $3^\circ$ . (d) is a Keplerian disk of thickness 1% of its radius. The bicones and disk models can be oriented by inclining them in a certain direction. The orientation is indicated for each model. RA indicates an anti-clockwise rotation on the plane of the magnification map.

### 3.4 Model slicing

Once a model has been generated with the appropriate velocity and emissivity profile, it is sliced by time to produce many profiles representing the progress of the flare. To find how microlensing changes the spectrum, each time slice must be further sliced by velocity. The resulting slice profiles are microlensed and the unlensed and lensed flux of the slice recorded. This produces a grid of values indexed by lensed/unlensed, time, and velocity. Spectra for flares can be implemented by selecting and combining values from the grid. For example, the lensed spectrum of the flaring BELR at time  $T$  is obtained by multiplying the lensed velocity slices for time  $T$  by  $k$ , and combining that with all other lensed grid values into a total flaring BELR spectrum.

Spectra for the quiescent BELR of Figure 3 are shown in Figure 4. These spectra are consistent with those reported in other works (e.g. Abajas et al. 2002), but not identical, because of the different radii, thicknesses, and other values used here.

We use 12 time intervals for the purpose of visualization. The flare is brightest in the early times, and also changes rapidly then, so the first two time intervals are shorter, i.e.

of higher time-resolution, than those that follow. The flare also has a small profile at the end of its life, and therefore possibly high microlensing variability, so the last two time intervals will be shorter than those preceding them. For a BELR of size  $0.06 \text{ pc}$  in Q2237+0305, a flare will have a duration of  $142.95 h_{70}^{-1/2} (M/M_\odot)$  days in the rest frame of the quasar. The lensed quasar in Q2237+0305 is located at a redshift of  $z_S = 1.695$ , so the flare will have a duration of  $385.26 h_{70}^{-1/2} (M/M_\odot)$  days in the observer's frame. Therefore we set  $T_{max} = 385$  days as the lifetime of a flare through our BELR models; the time intervals begin at 0, 0.05, 0.1, 0.2 ... 0.8, 0.9, 0.95 of  $T_{max}$ . All the material that is flaring within the time interval will be used to form a brightness profile for that interval. For the spectra we use 40 velocity slices within each time slice, a value chosen to give good velocity resolution for data analysis and visualization. The velocities are normalized to be between -1 and 1 regardless of the profile's orientation.

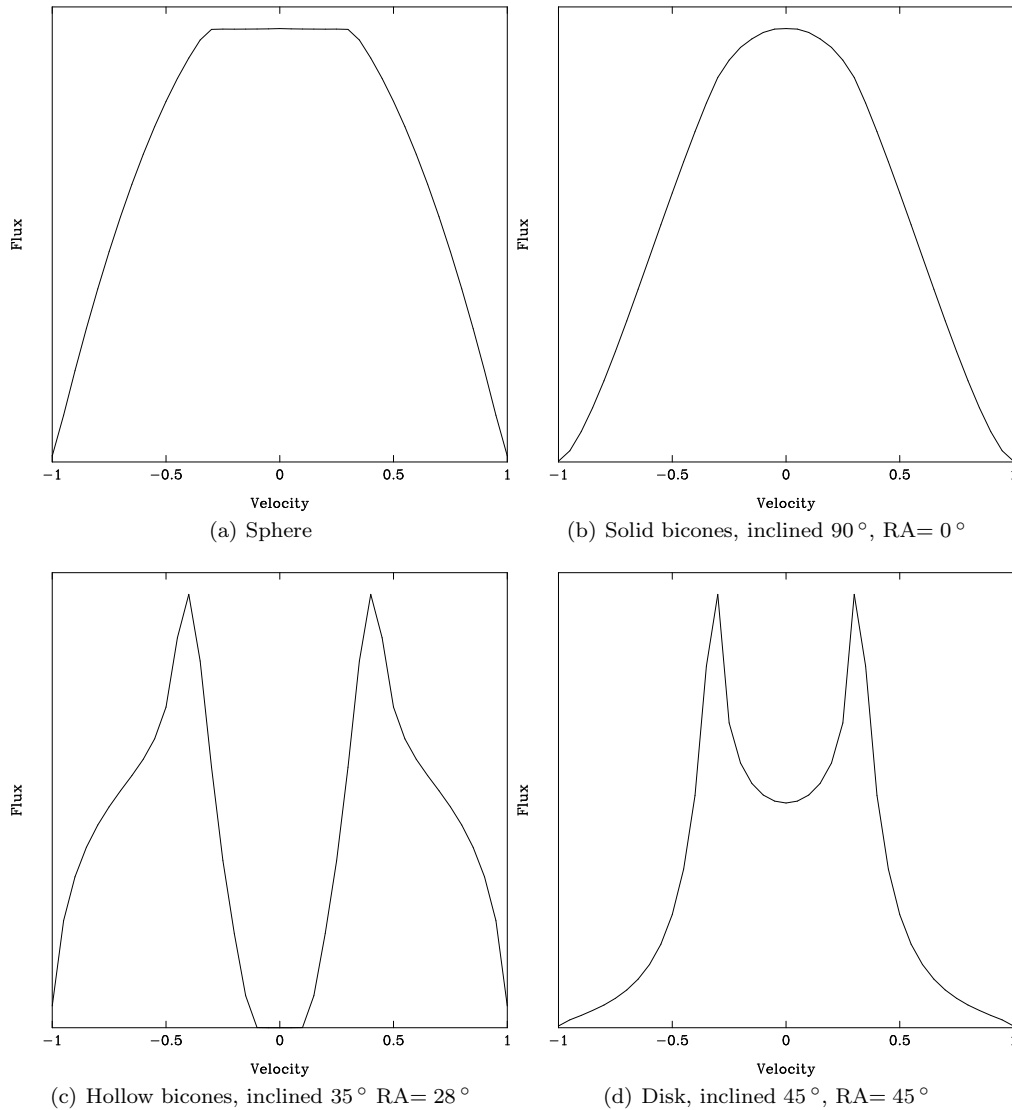


**Figure 4.** The spectra for the oriented source models shown in Figure 3. Velocities are normalized to -1 to 1 for each model regardless of orientation. The flux is a normalized value which is not shown, only the spectrum shape is significant.

### 3.5 Model orientations and map location

In this paper we will not attempt to present statistical results for many orientations and locations, but focus on the behaviour for a simple situation, thus demonstrating the method and indicating possible fruitful directions of investigation. Figure 6 shows the source models with the orientations we have chosen, superimposed on the magnification map at the location we have chosen. The sources lie over a region between two caustics where the magnification is increased; note that the material close to the center of the BELR, which has the highest emission, will be magnified more than the outlying material. The caustics will be referred to as the left and right caustics, i.e. as they appear on the map. Some of the profiles extend to the bottom right where the right caustic proceeds towards a cusp. The orientations that we use are either wholly face-on ( $0^\circ$  inclination) or mostly side-on:  $60^\circ$  inclination. The disk when face-on (Figure 6 (f)) has no line-of-sight velocity, therefore

it is at  $10^\circ$  inclination so it has some line-of-sight velocity components.

## 4 QUALITATIVE RESULTS

We present source profiles and spectra of a BELR as a flare progresses through it. Figure 7 shows the source brightness profile of a flare propagating through the spherical inflow BELR (Figure 3(a)). The profiles are superimposed over the outline of the caustic structure from the magnification map. Each column shows the BELR profile sliced by velocity, each row shows the profile within a time interval. The velocity bin for each column has a width of 0.2, beginning at -1, -0.8, -0.6, ... 0.8, from left to right column. The first row shows the BELR before the flare begins, i.e. the quiescent BELR. The time intervals for the subsequent rows, reading down the Figure, begin at 0, 0.05, 0.1, 0.2 ... 0.9, 0.95 of  $T_{max}$ , the lifetime of the flare. The image intensity indicates the amount of emission, so that the flare is visible as dark

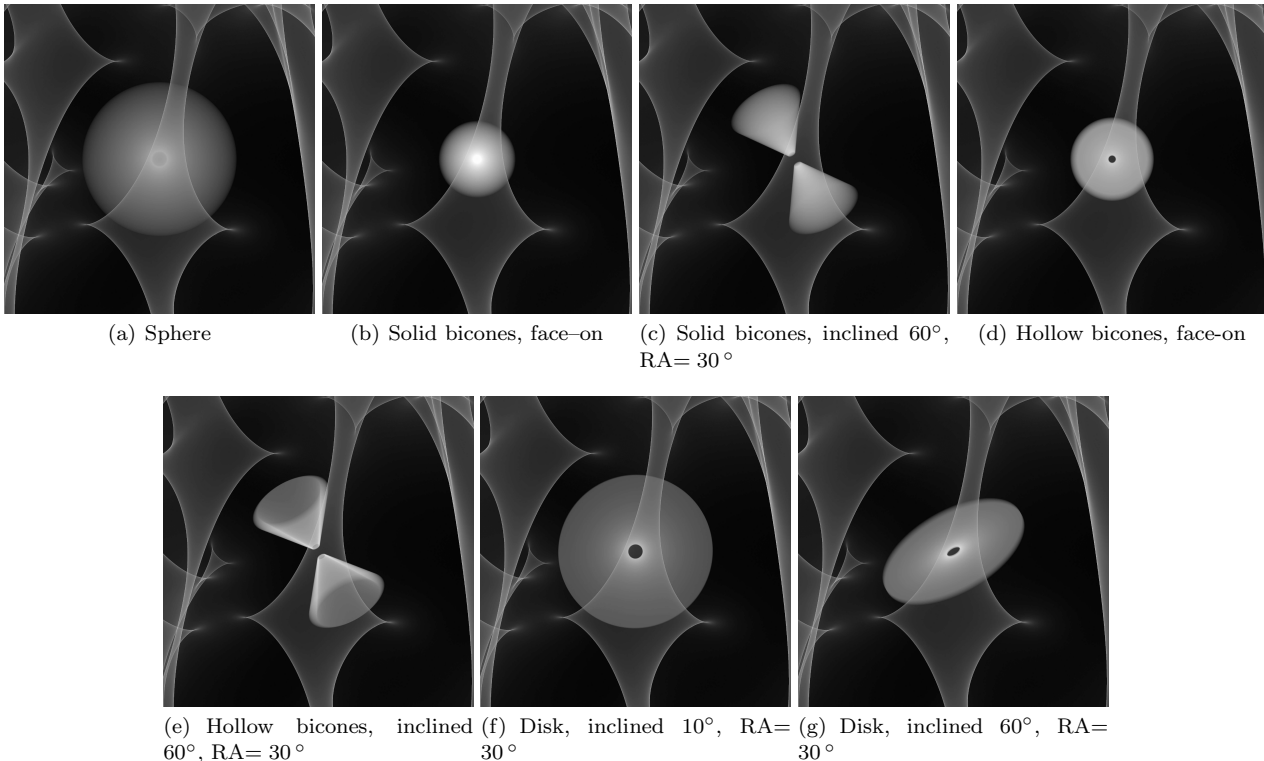


**Figure 6.** Source profiles superimposed on a location of the map shown in Figure 2. These are the profiles and magnification map location used to generate the data in this paper. Note that the orientations are not the same as Figure 3. The models have a radius of 0.06 pc (1 ER); the section of the map that is shown here has a width of 0.24 pc (4 ER). The disk is rotating clockwise so that the bottom-left is towards the observer (blue-shifted, negative velocities).

patches, note the flare has been rescaled in the images for ease of visualization. The two numbers in each box show the central velocity and time of the BELR material in the image. The right-most column is the unlensed and lensed spectrum of the flaring BELR in the row, constructed from 40 velocity bins, i.e. a higher resolution than can be shown in the source profiles. The spectrum in blue is the unlensed spectrum, the lensed spectrum is in red. The lensed spectrum has been scaled to the mean magnification of image A, for comparison with the unlensed. The spectrum velocities, indicated on the horizontal axis of the bottom spectra, are normalised values from -1 to 1. The flux values (vertical axis) are arbitrary and are not indicated. Figures 8 – 13 show the flaring BELR for the other source models.

## 5 DISCUSSION

Of interest is the comparison of the unlensed and lensed spectrum as the flare propagates, and whether that can be used to differentiate between BELR models, and their orientations. Here we will present a description of the spectra for the various source models at the location and orientations we have chosen. By using a single location with simple caustic structure we demonstrate that microlensing can alter the spectrum of a flare in the BELR, and the sorts of signatures we might expect to see. Future contributions will provide a comprehensive analysis describing the microlensing behaviour for many locations on the magnification map.

**Table 1.** Total magnification of the sources after microlensing, at the location chosen (Figure 6).

| Profile                            | Magnification |
|------------------------------------|---------------|
| Sphere                             | 0.75          |
| Bicones inclined $0^\circ$         | 0.93          |
| Bicones inclined $60^\circ$        | 0.70          |
| Hollow bicones inclined $0^\circ$  | 0.86          |
| Hollow bicones inclined $60^\circ$ | 0.74          |
| Disk inclined $10^\circ$           | 0.72          |
| Disk inclined $60^\circ$           | 0.76          |

### 5.1 Comments on the microlensing of the quiescent BELR profiles

At the location chosen, the source is demagnified relative to the mean magnification; Table 1 lists the magnifications for the various profiles, scaled to the mean of image A. The magnifications are around 0.75, except for the face on cones, which are higher because most of the flux for these profiles sits within the high magnification region (Figure 6). The spectra for the microlensing of the profiles are in the top row, last column, of Figures 7 – 13. In all cases the lensed spectrum retains a similar shape to the unlensed spectrum. The inclined solid bicones (Figure 9) have more material towards the ends, which counters the decline in emissivity, and the spectrum has a rounded peak. The spike at 0 velocity for the inclined hollow cones (Figure 11) is due to their orientation: with an opening angle of  $30^\circ$  and an inclination of

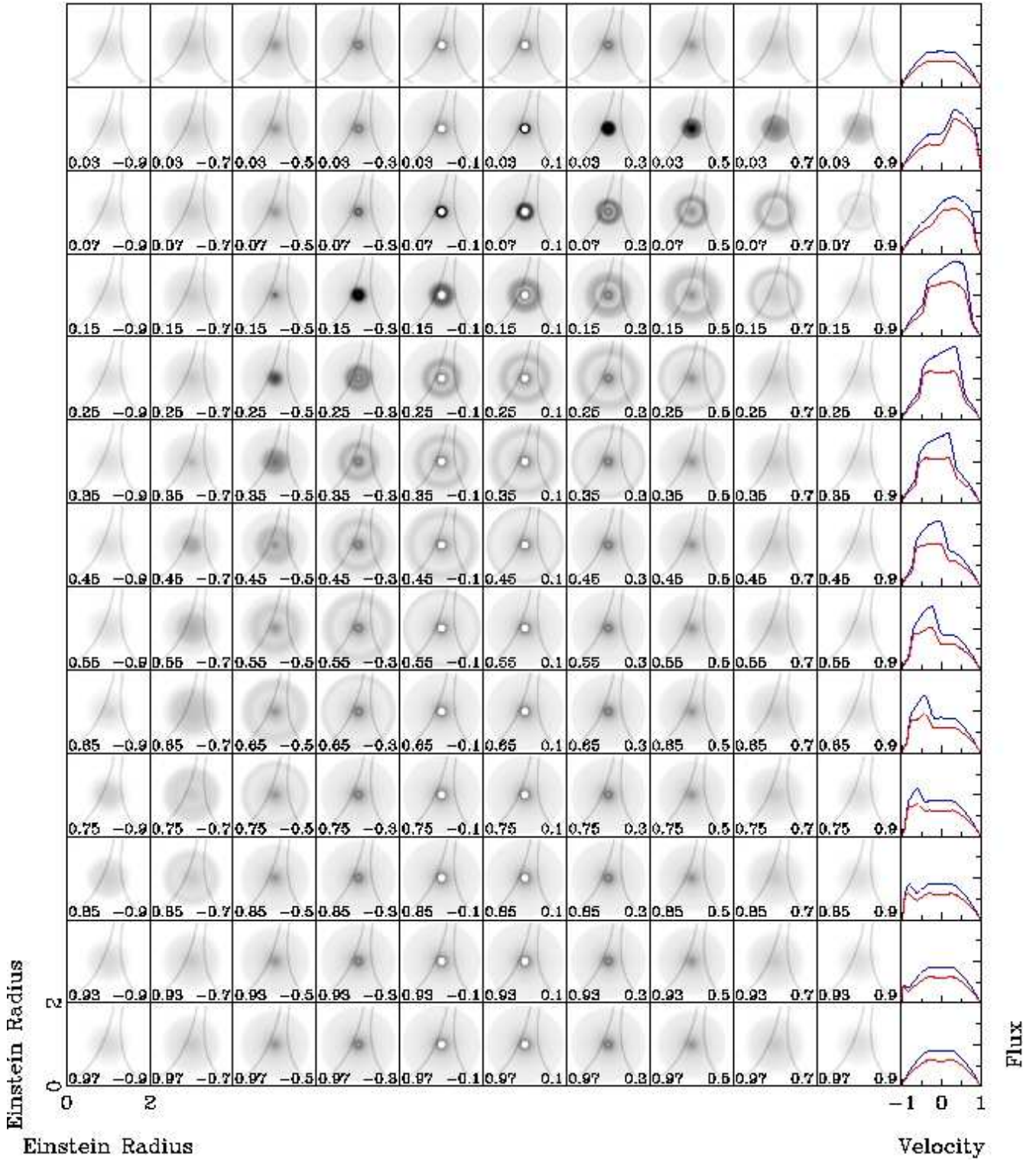


**Figure 7.** Images of the surface brightness profiles (first 10 columns) and spectra (last column) of the spherical inflowing BELR (Figure 6(a)) as a flare propagates through it. The profiles are superimposed over the outline of the caustic structure from the magnification map. The images are time and velocity sliced profiles of the BELR; the first number in a BELR image is the central time, normalized to  $T_{max}$ , of the time interval, the second number is the central velocity of the velocity interval. The first 10 columns contain the BELR profile velocities in slices of 0.2, beginning at -1, -0.8, -0.6, ... 0.8, 1, from left to right. The first row shows the quiescent BELR. Subsequent rows, reading down the page, show the flaring BELR sliced into time intervals beginning at 0, 0.05, 0.1, 0.2, 0.3 ... 0.8, 0.9, 0.95 of  $T_{max}$ . The flaring material appears darker than the rest of the BELR; note that it has been rescaled for enhanced visualization in the profiles. The column on the right shows the spectrum of the BELR, the blue line is the unlensed spectrum, and the red line is the lensed spectrum. The lensed spectra have been scaled relative to the mean magnification, for comparison with the unlensed. Each spectrum in a row is the spectrum of the flaring BELR for the time interval of the row. Note how the flare appears at high positive velocities (right), and over time (down the page) migrates to negative velocities; this is also tracked in the spectra.

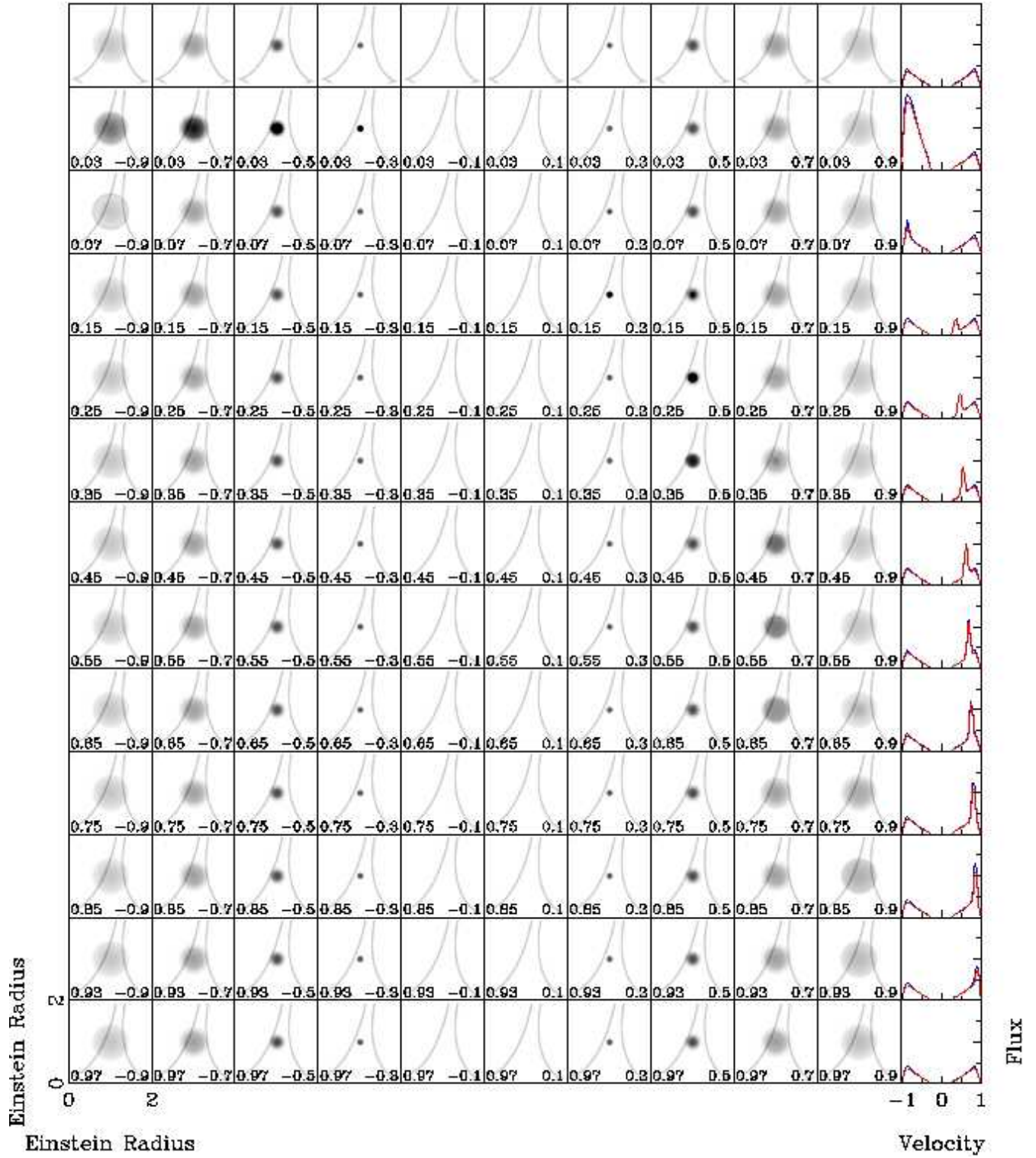
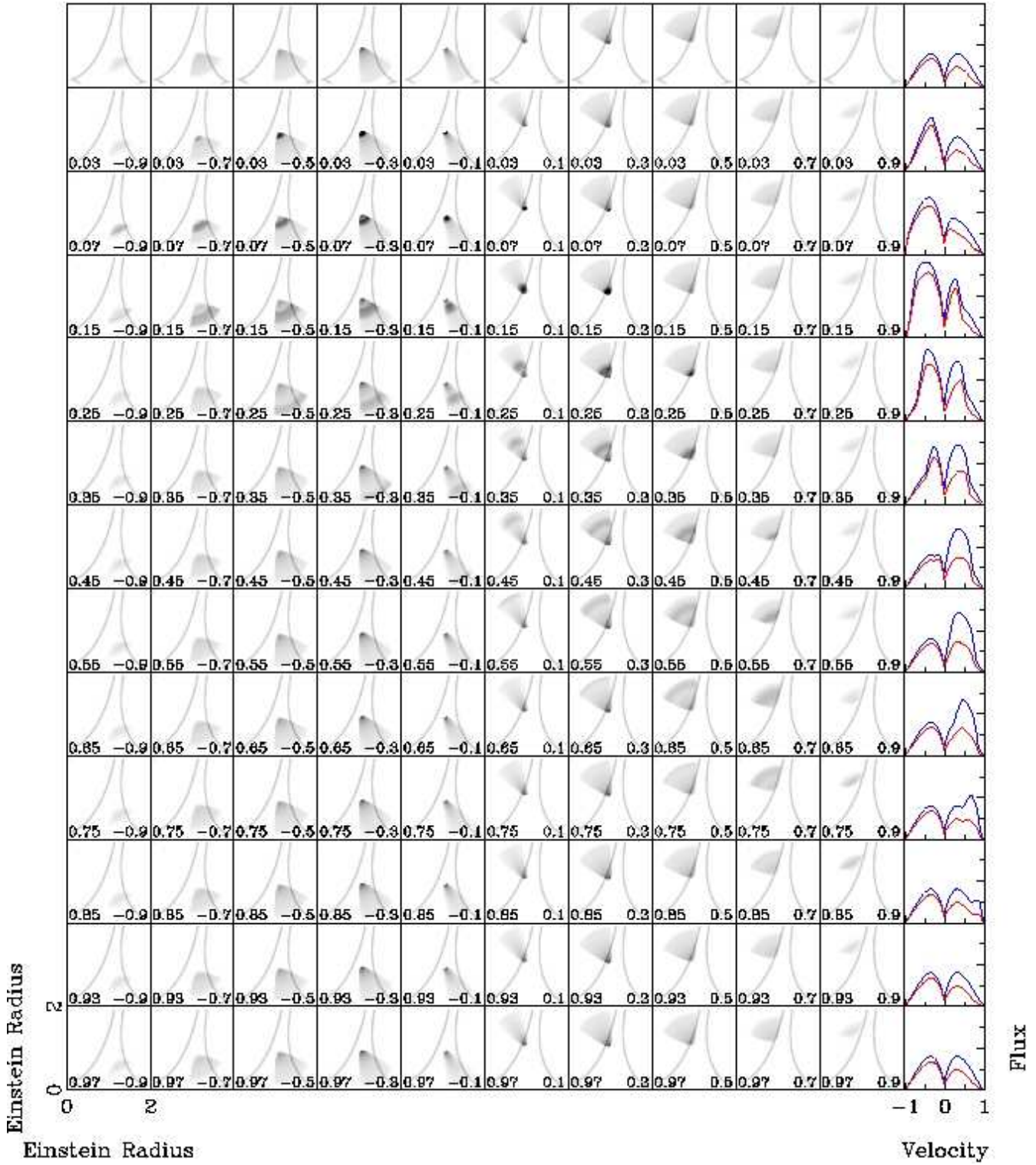


Figure 8. As for Figure 7, but the source model is the face-on solid bicones (Figure 6(b)).

$60^\circ$ , each cone has an edge that is lying flat along the plane of the sky, the material there has 0 line-of-sight velocity.

## 5.2 Comments on the effect of the flare

Now we turn to the other rows in Figures 7 – 13, those that display the behaviour of the flare. Where necessary we will refer to the row by its central time, eg.  $T=0.07$ , and column by central velocity, eg.  $V=0.5$ . Some of the spectra



**Figure 9.** As for Figure 7, but the source model is the side-on solid bicones (Figure 6(c)).

show effects caused by the microlensing of the flare, we will highlight and discuss the interesting ones.

The sphere and the face-on bicones do not show much difference between the unlensed and lensed spectrum over time, because of the symmetries in these models. Blue- and redshifted material is spatially co-located at each point of

the profile, and also at a range of velocities between the extremes of -1 to 1. This means there will be little differential microlensing. A small effect in the sphere (Figure 7) is the enhanced sharpness of the peak at  $T=0.75$  in the lensed spectrum at  $V=-0.8$ , which occurs because the flare is small at this point and passes over the left caustic, near the top left

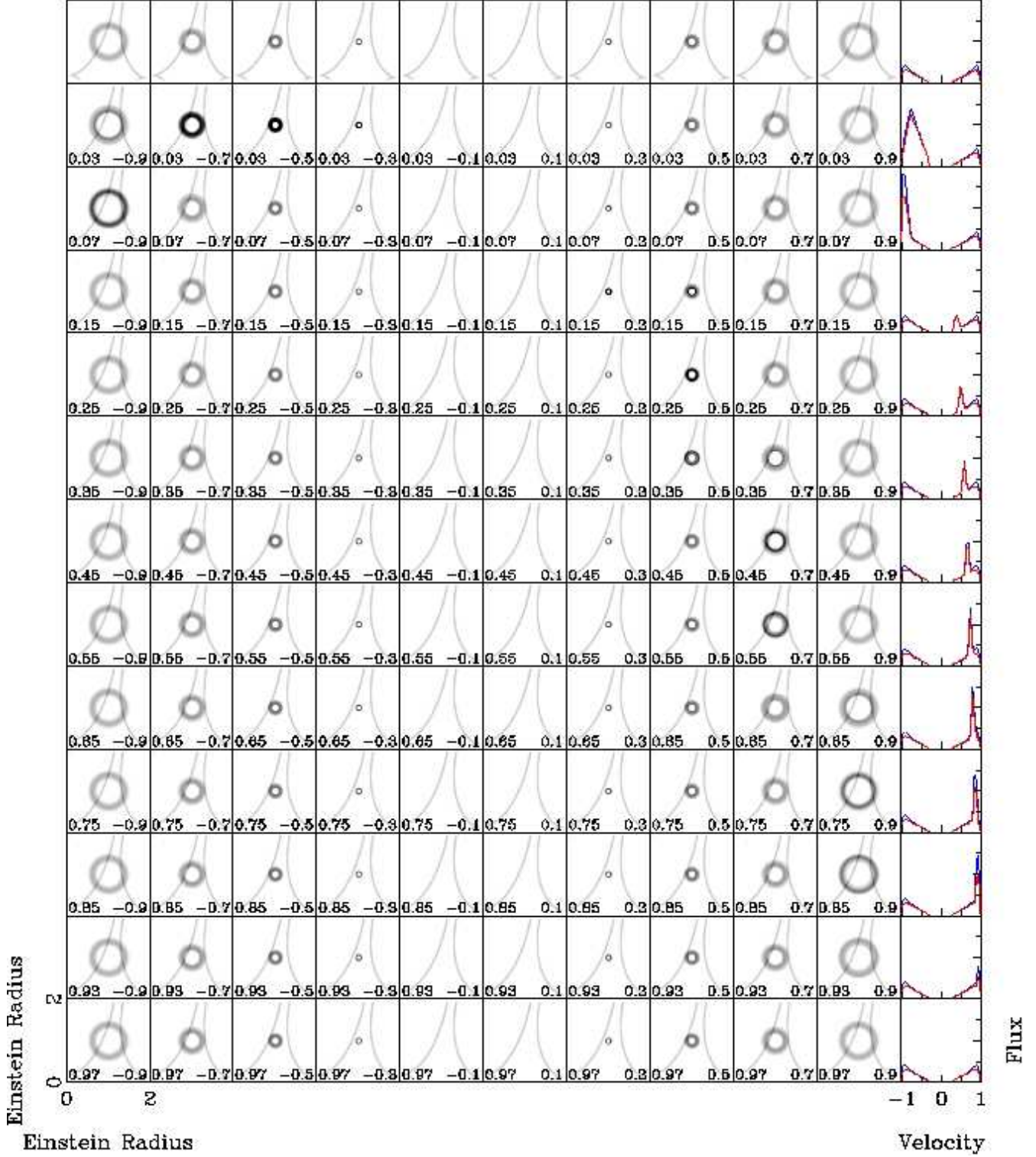


**Figure 10.** As for Figure 7, but the source model is the face-on hollow bicones (Figure 6(d)).

of the sphere inner radius. There are some effects with the hollow bicones (Figure 10), due to the cone edge lying over a caustic. As the flare moves down the edges of the face-on cone it produces a peak at negative velocities, at  $T=0.03$ - $0.07$ , which is diminished in the lensed spectra because some material lies outside the left caustic. As the flare moves off

the cone edge and inside the caustics, the peak disappears in both spectra and they become similar at the negative end ( $T=0.35$ ). Corresponding behaviour can be seen in positive velocities from  $T=0.15$  as the flare travels along the edge of the away-facing cone.

The inclined bicones produce more interesting effects

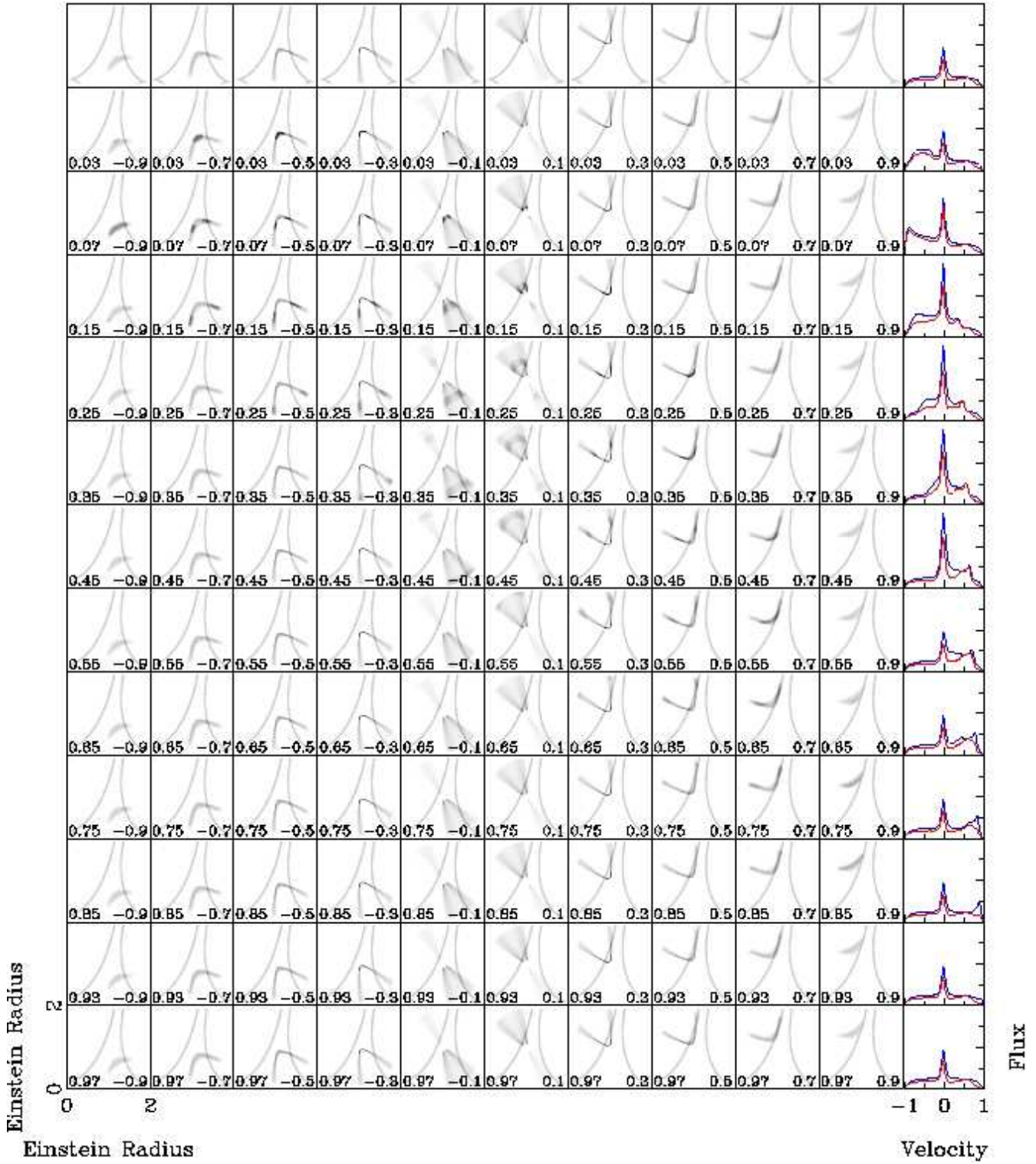
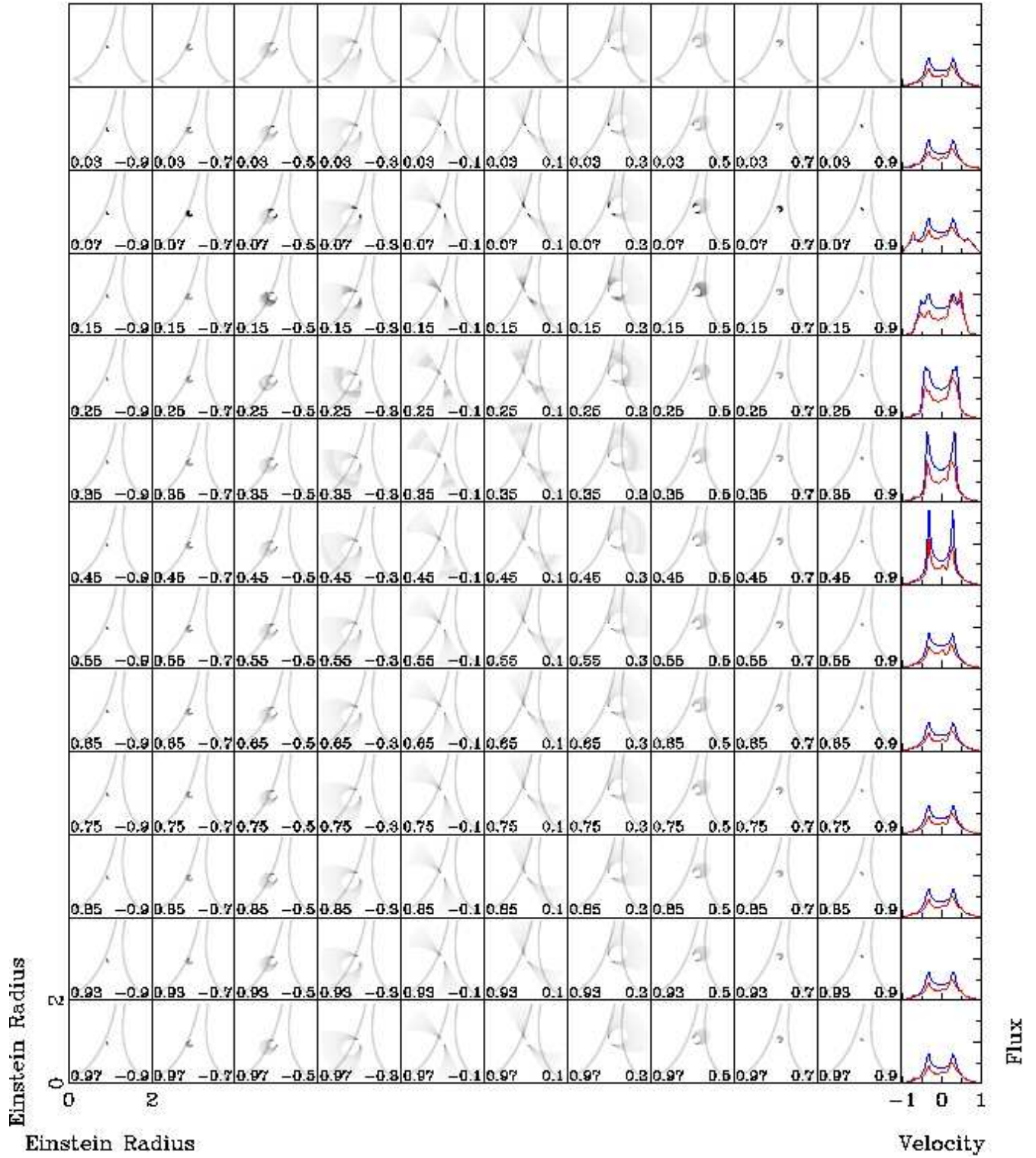


Figure 11. As for Figure 7, but the source model is the side-on hollow bicones (Figure 6(e)).

due the flare passing over caustics. The “kink” at  $T=0.15$ ,  $V=0.5$  in the lensed spectrum for the inclined solid bicones (Figure 9) is not a drop at high velocities but a raising of lower velocities, because the flare is sitting on the left caustic near the base of the red-shifted cone, and low positive velocities are magnified. Similarly, the “dimple” in the peak

at positive velocities for  $T=0.75-0.85$  is really a second peak around  $V=0.6$ . At this time interval the surface of the flare cuts down and partly away from the observer, through the redshifted cone. The distant side of the cone (as viewed by the observer) has faster positive velocities, and some of this material is near the left caustic, and therefore magnified.



**Figure 12.** As for Figure 7, but the source model is the almost-face-on disk (Figure 6(f)).

As with the solid bicones, the flare in the hollow bicones (Figure 11) lifts both the lensed and unlensed spectra at the negative end, but by  $T=0.25$  the lensed flux has dropped. At  $T=0.15$ ,  $V=-0.5$  the source profile consists of two edges and the flare is on both of them, but one is outside the high magnification region, leading to the drop in flux. A similar

effect occurs at positive velocities where only one of the two edges of the away-facing cone is close to the left caustic.

Both face-on and inclined disk profiles produce effects. In the face-on disk spectra (Figure 12) at  $T=0.07$ , the flare is in small regions lying on both caustics, so multiple small peaks are produced in the lensed spectrum. By  $T=0.25$  these

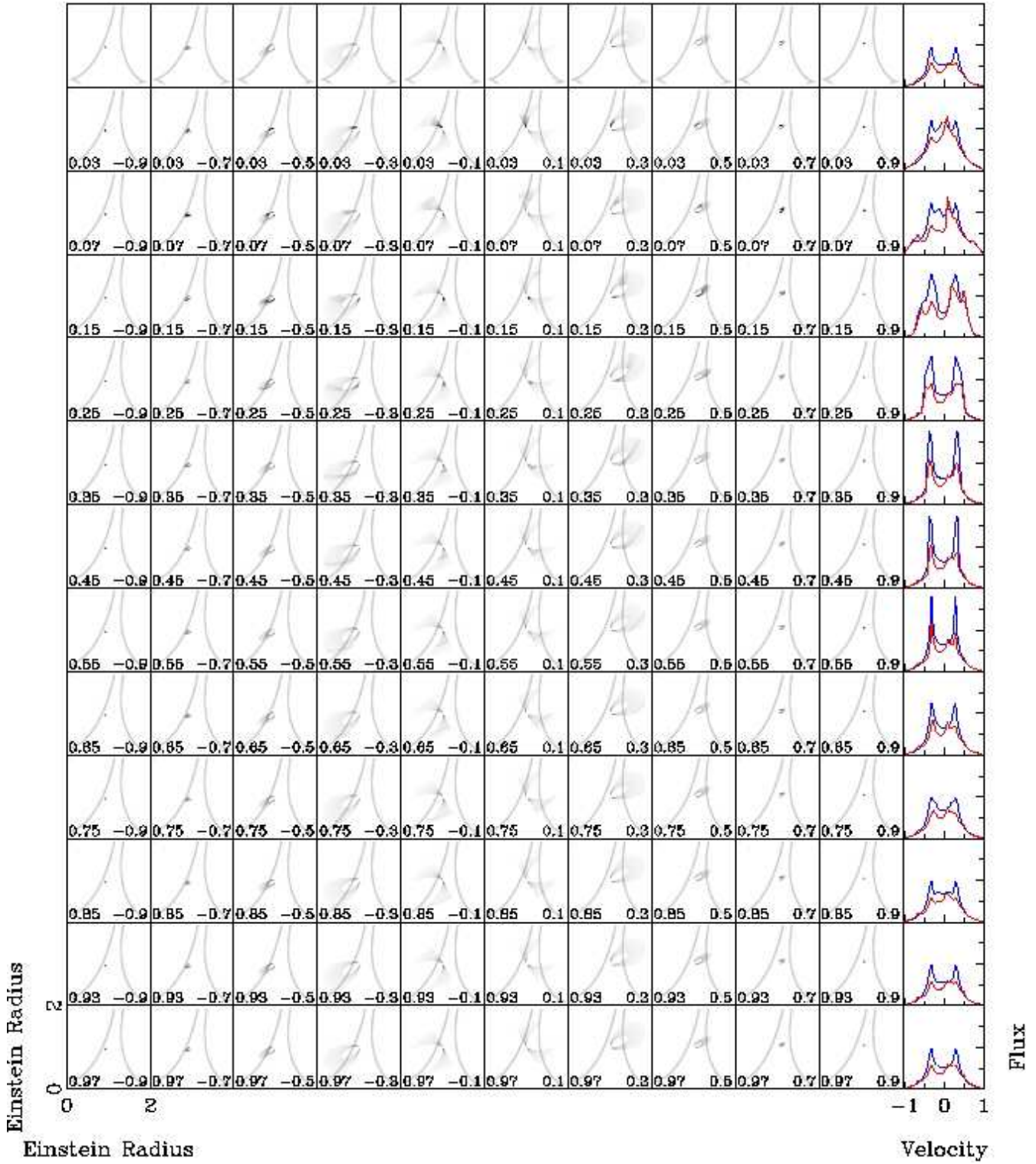
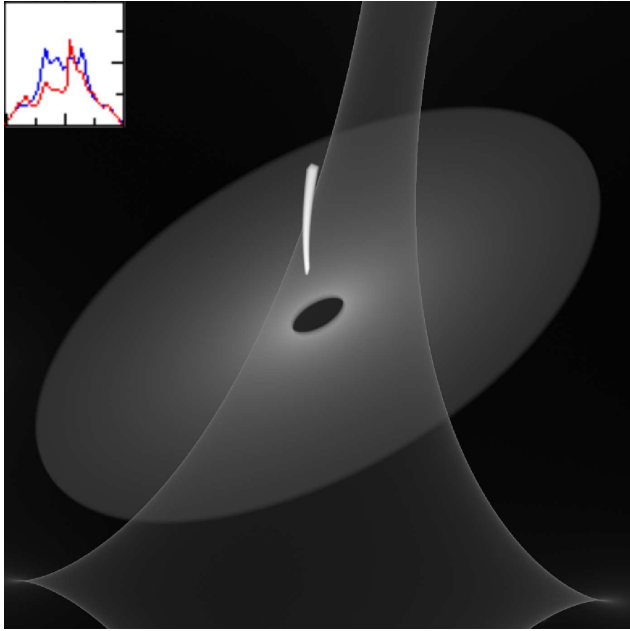


Figure 13. As for Figure 7, but the source model is the side-on disk (Figure 6(g)).

peaks have disappeared and at negative velocities the lensed spectrum is diminished because the blue-shifted half of the disk, particularly that close to the core, is less magnified. Of interest in the inclined disk (Figure 13), and the most significant effect presented here, is the large spike at small positive velocities at  $T=0.03-0.15$ . This is due to the flare

reaching some disk material at points just after it has turned over from negative to positive velocities, where it is sitting on a caustic, and highly magnified. This material can be seen in Figure 14 inside the inclined disk, and is brightened in the disk for visualization purposes. The material lies within the time interval  $T=0.05-0.1$ , and within velocities of  $0.08 \leq$



**Figure 14.** Showing the flaring material in the inclined disk (Figure 6(g)) at  $T=0.05-0.1$  and velocity  $0.08 \leq V \leq 0.09$ , superimposed on the map. The region of the map shown has width 0.12 pc (2 ER). The flare material is brightened relative to the rest of the disk, for visualization, and is shown in white. The spectrum from row  $T=0.07$ , Figure 13, in which there is a high magnification spike produced by this material, is shown at the top left. The material is highly magnified because it sits on a caustic.

$V \leq 0.09$ . The spectrum from row  $T=0.07$  Figure 13, in which the spike produced by this material lies, is shown at the top left of Figure 14. This spike is an example of a strong effect that occurs when microlensing and flaring are combined. At  $T=0.25$  the spike flattens, due to the flare passing over the inner edge of the disk which is near the left caustic.

## 6 CONCLUSIONS

In this paper we have demonstrated how the microlensing of a flare in a BELR can be modelled and analysed, and some of the effects that may be observed when a flaring BELR is microlensed. It is clear that the behaviour will be determined by several different parameters. Those that have been studied previously include the source model, and the emission and velocity profiles. When a BELR is flaring our investigations indicate that the following will also be important:

**Strength of the flare.** We have chosen a flare that increases the total flux by a moderate amount in the early stages ( $\sim 50\%$  in the sphere). The stronger the flare is, compared to the total BELR flux, the more noticeable it is, and the easier it will be to study as it is microlensed.

**Temporal asymmetry of the flare.** The variation in brightness of the flare over time depends on the source model and orientation. However, making use of this would require intensive monitoring during the flare lifetime because variation can occur rapidly, particularly at the beginning of the flare, where it will be most indicative of the model.

**Source shape with respect to the flare.** The flare in the spherical BELR is observed on the sky as an expanding and then diminishing circle. When overlaid on other source profiles the flare can break up into multiple regions, and this can produce structure in the spectrum if those regions have different velocities and different magnifications.

**High magnification regions with respect to the flare.** If the flare passes over a high magnification region of comparable size, like a caustic, this can cause a spike in the lensed spectrum. Therefore different locations will produce different microlensing behaviour due to the flare, as well as due to the source profile.

In most cases we have noticed that, at a first-order approximation, lensing does not change the shape of the flaring BELR spectrum as the flare progresses. Sources that will exhibit some variability can be characterised as:

- having blue and redshifted material spatially separated on the sky,
- not uniform, having internal structure, such as edges,
- oriented so that the flare spreads asymmetrically over the profile over time,
- oriented so that the flare passes over high magnification regions of similar size to the flare.

We have found, at least at the source location of Figure 6, that side-on orientations have produced most variability. Q2337+0305 may therefore not be an appropriate system for microlensing studies of flaring BELRs, as Poindexter & Kochanek (2010) have determined the quasar is inclined by only  $\sim 35^\circ$  (in our convention) and hence is mostly face-on. Also, Q2237+0305 will produce microlensing variability that occurs within the duration of the flare, due to the short time-scale of events in Q2237+0305, which will complicate the analysis.

A comprehensive quantitative analysis will determine to what extent different models, and their orientations, can be differentiated. We intend to characterize the change in spectra and total magnification of the BELR, as a flare passes through it, using a small number of parameters based on simple statistics or feature extraction. Of particular importance will also be the uncorrelated microlensing variations between the four images in Q2237+0305, which may produce the most significant means of differentiating between sources. Since the location of the observed flare in the BELR profile may lie over caustics, and the caustic structure will not be identical at that location for each image, there will certainly be differences in the behaviour between the images. A statistical analysis will indicate how well the microlensing between the images can differentiate the BELR models during a flare, how often this may happen, what to use as an observing trigger, and what to look for in the light curves and spectra of the images during the event.

## ACKNOWLEDGMENTS

We thank the anonymous reviewer for their comments which improved the quality and content of this paper. This work was supported by the High Performance Computing Facility at The University of Sydney and the NCI National Facility at the ANU. Hugh Garsden acknowledges funding support

from an Australian Postgraduate Award. This work is undertaken as part of the Commonwealth Cosmology Initiative (www.thecci.org), and funded by the Australian Research Council Discovery Project DP0665574.

## REFERENCES

- Abajas C., Mediavilla E., Muñoz J. A., Popović, L. Č., & Oscoz, A., 2002, *ApJ*, 576, 640
- Abajas C., Mediavilla E., Muñoz J. A., Gómez-Álvarez P., Gil-Merino R., 2007, *ApJ*, 658, 748
- Bate N. F., Webster R. L., Wyithe J. S. B., 2007, *MNRAS*, 381, 1591
- Bentz M. C., et al., 2008, *ApJL*, 689, L21
- Bentz M. C., et al., 2009, *ApJ*, 705, 199
- Bentz M. C., et al., 2010, *ApJL*, 720, L46
- Blandford R. D., McKee C. F., 1982, *ApJ*, 255, 419
- Brewer B. J., et al., 2011, *ApJL*, 733, L33
- Chelouche D., Daniel E., 2011, *arXiv*, arXiv:1105.5312
- Denney K. D., et al., 2009, *ApJL*, 704, L80
- Dye S., Evans N. W., Belokurov V., Warren S. J., Hewett P., 2008, *MNRAS*, 388, 384
- Elvis M., 2000, *NewAR*, 44, 559
- Garsden H., Lewis G. F., 2010, *NewA*, 15, 181
- Gómez-Álvarez P., Mediavilla E., Muñoz J. A., Arribas S., Sánchez S. F., Oscoz A., Prada F., Serra-Ricart M., 2006, *ApJ*, 645, L5
- Horne K., Peterson B. M., Collier S. J., Netzer H., 2004, *PASP*, 116, 465
- Huchra J., Gorenstein M., Kent S., Shapiro, I., Smith G., Horine E., Perley R., 1985, *AJ*, 90, 691
- Inada N., et al., 2005, *AJ*, 130, 1967
- Kaspi S., Brandt W. N., Maoz D., Netzer H., Schneider D. P., Shemmer O., 2007, *ApJ*, 659, 997
- Kayo I., Inada N., Oguri M., et al., 2010, *AJ*, 139, 1614
- Kayser R., Refsdal S., 1989, *Natur*, 338, 745
- Keeton C. R., Burles S., Schechter P. L., Wambsganss J., 2006, *ApJ*, 639, 1
- Lamer G., Schwope A., Wisotzki L., Christensen L., 2006, *A&A*, 454, 493
- Lewis G. F., Irwin M. J., Hewett P. C., Foltz C. B., 1998, *MNRAS*, 295, 573
- Lewis G. F., Ibata R. A., 2004, *MNRAS*, 348, 24
- Lewis G. F., Ibata R. A., 2006, *MNRAS*, 367, 1217
- Mortonson M. J., Schechter P. L., Wambsganss J., 2005, *ApJ*, 628, 594
- Mosquera A. M., Muñoz J. A., Mediavilla E., *ApJ*, 2009, 691, 1292
- Mosquera A. M., Kochanek C. S., 2011, *arXiv*, arXiv:1104.2356
- Myers S. T., et al., 1999, *AJ*, 117, 2565
- Nemiroff R. J., 1988, *ApJ*, 335, 593
- Ota N., et al., 2006, *ApJ*, 647, 215
- O'Dowd M., Bate N. F., Webster R. L., Wayth R., Labrie K., 2011, *MNRAS*, 415, 1365
- Pancoast A., Brewer B. J., Treu T., 2011, *ApJ*, 730, 139
- Peterson B. M., 1993, *PASP*, 105, 247
- Peterson B. M., 1997, *An introduction to active galactic nuclei*. Cambridge Univ. Press, Cambridge
- Peterson B. M., et al., 2004, *ApJ*, 613, 682
- Peterson B. M., 2006, *LNP*, 693, 77
- Poindexter S., Kochanek C. S., 2010, *ApJ*, 712, 668
- Richards G. T., et al., 2004, *ApJ*, 610, 679
- Robinson, A., 1995, *MNRAS*, 272, 647
- Schmidt R., Webster R. L., Lewis G. F., 1998, *MNRAS*, 295, 488
- Schneider P., Wambsganss J., 1990, *A&A*, 237, 42
- Shalyapin V. N., 2001, *AstL*, 27, 150
- Sluse D., Schmidt R., Courbin F., Hutsemékers D., Meylan G., Eigenbrod A., Anguita T., Agol E., Wambsganss J., 2011, *A&A*, 528, A100
- Turner E. L. et al., 1989, *BAAS*, 21, 718
- Udalski A., Szymanski M. K., Soszynski I., Poleski R., 2008, *AcA*, 58, 69
- Walsh D., Carswell R. F., Weymann R. J., 1979, *Natur*, 279, 381
- Wambsganss J., 1990, Ph.D. Thesis, Ludwig Maximilian University, Munich.
- Wambsganss J., Paczynski B., 1991, *AJ*, 102, 864
- Wambsganss J., 1999, *JComAM*, 109, 353
- Wyithe J. S. B., Webster R. L., Turner E. L., 2000, *MNRAS*, 318, 762
- Wayth, R. B., O'Dowd, M., Webster, R. L., 2005, *MNRAS*, 359, 561

This paper has been typeset from a  $\text{\LaTeX}$  file prepared by the author.